Multi-valley superconductivity in ion-gated MoS_2 layers

E. Piatti,[1,*] D. De Fazio,[2,*] D. Daghero,[1] S. R. Tamalampudi,[2] D. Yoon,[2] A. C. Ferrari,[2] and R. S. Gonnelli[1,†]

[1] *Department of Applied Science and Technology, Politecnico di Torino, 10129 Torino, Italy*
[2] *Cambridge Graphene Centre, University of Cambridge, Cambridge CB3 OFA, UK*

Layers of transition metal dichalcogenides (TMDs) conjugate the enhanced effects of correlations associated to the two-dimensional limit with electrostatic control over their phase transitions by means of an electric field. Several semiconducting TMDs, such as MoS_2, develop superconductivity (SC) at their surface when doped with an electrostatic field, but the mechanism is still debated. It is often assumed that Cooper pairs reside only in the two electron pockets at the K/K' points of the Brillouin Zone. However, experimental and theoretical results suggest that a multi-valley Fermi surface (FS) is associated with the SC state, involving 6 electron pockets at the Q/Q' points. Here, we perform low-temperature transport measurements in ion-gated MoS_2 flakes. We show that a fully multi-valley FS is associated with the SC onset. The Q/Q' valleys fill for doping$\gtrsim 2\cdot10^{13}$cm^{-2}, and the SC transition does not appear until the Fermi level crosses both spin-orbit split sub-bands Q_1 and Q_2. The SC state is associated to the FS connectivity and promoted by a Lifshitz transition due to the simultaneous population of multiple electron pockets. This FS topology will serve as a guideline in the quest for new superconductors.

INTRODUCTION

Transition metal dichalcogenides (TMDs) are layered compounds that show a range of electronic properties. Depending on chemical composition, crystalline structure, number of layers (N), doping, and strain, different TMDs can be semiconducting, metallic and superconducting[1]. Amongst semiconducting TMDs, MoS_2, $MoSe_2$, WS_2 and WSe_2 have sizeable bandgaps in the range$\sim$1-2eV[2]. When exfoliated from bulk to single layer (1L), they undergo an indirect-to-direct gap transition[2–4], hence offering a platform for various electronic and optoelectronic applications[1, 2, 5], such as transistors[6–8], photodetectors[9–12], modulators[13] and electroluminescent devices[14, 15].

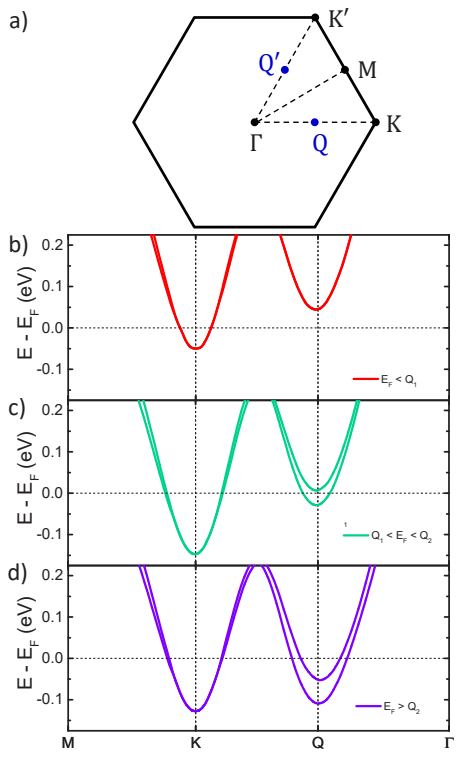

FIG. 1: a) BZ for the 2H crystal structure. High symmetry points Γ, M, K, K', and points Q and Q' are highlighted. b-d) 3L-MoS_2 band structure for 3 doping values. Positions and values of the energy minima are taken from Ref.16. The valleys at K/K' have two spin-orbit split sub-bands, with split much smaller than at Q/Q', not seen in this scale.

For all TMDs with 2H crystal structure, the hexagonal Brillouin Zone (BZ) features high-symmetry points Γ, M, K and K'[4, 16], Fig.1a. The minima of the conduction band fall at K and K' and at Q and Q', approximately half-way along the Γ-K (K') directions[4, 16],Fig.1a. In absence of an out-of-plane electric field, the relative position of the two latter minima depends on N and strain[4, 16, 17]. The global minimum of the conduction band sits at K/K' in 1L-MoS_2 and at Q/Q' in few layer (FL)-MoS_2 with N$\geq$4[4]. When an electric field is applied perpendicular to the MoS_2 plane, inversion symmetry is broken and the global minimum of the conduction band is shifted to K/K' in any FL-MoS_2 as well[16], Figs.1b-d. The valleys at K/K' and at Q/Q' are characterized by a different electron-phonon coupling (EPC)[18] and, when inversion symmetry is broken, by a different spin-orbit coupling (SOC)[19]. In particular, both EPC and SOC are larger in the Q/Q' valleys[18, 19].

The field-effect transistor (FET) architecture is ideally suited to control the electronic properties of 1L flakes, as it simultaneously provides an electrostatic control of the transverse electric field and the carrier density. In the electric-double-layer (EDL) technique[20], the standard solid gate dielectric is replaced by an ionic medium, such as an ionic liquid or electrolyte. In this configuration, the EDL that forms at the ionic liquid/electrode interfaces supports electric fields in excess of$\sim$10MV/cm[21], corre-

sponding to surface carrier densities $n_{2d} \gtrsim 10^{14}\text{cm}^{-2}$[21]. Ionic-liquid gating has been used to tune the Fermi level, E_F, in TMDs and explore transport at different carrier concentrations[22–26]. The vibrational properties of TMDs can also be controlled by means of the EDL technique, as suggested by gate-induced softening of Raman-active modes in 1L-MoS_2[27], while the opposite is observed in gated 1L[28] and two-layer (2L)[29] graphene. Ref.[23] reported a gate-induced superconducting state at the surface of liquid-gated MoS_2 flakes with N$\gtrsim$25[23], while Ref.34 detected this down to N=1.

Most of these results have been interpreted in terms of the population of the conduction band minima at K/K'[23, 32, 33, 46], which are the global minima in both 1L-MoS_2[3, 18] and electrostatically-doped FL-MoS_2[16, 23, 32, 33], Fig.1b. Theoretical investigations however suggested that the population of the high-energy minima at Q/Q' may have an important role in determining the properties of gated MoS_2 flakes, by providing contributions both to EPC[16, 18] and SOC[19, 44]. Ref.18 predicted that when the Q/Q' valleys of 1L-MoS_2 are populated (Fig.1c,d), EPC strongly increases (from$\sim$0.1 to $\sim$ 18), leading to a superconducting transition temperature $T_c \sim 20$K for a doping level $x = 0.18$ electrons(e^-)/unit cell (corresponding to $E_F = 0.18 \pm 0.02$eV at K/K' and 0.08 ± 0.02eV at Q/Q')[16]). However, Ref.34 measured $T_c \simeq 2$K for $x \simeq 0.09 \div 0.17$ e^-/unit cell in e^--doped 1L-MoS_2. This quantitative mismatch may be associated to the contribution of e^--e^- interactions, whose role in the determination of T_c is still under debate[40, 41]. Overall, the qualitative agreement between the model of Ref.18 and the trend of T_c with e^- doping in Ref.23 suggests that the mechanism of Ref.18 for EPC enhancement when the Q/Q' valleys are crossed may also hold for FL-MoS_2.

Inversion symmetry can be broken in MoS_2 either by going to the 1L limit[18], or by applying a transverse electric field[30, 31]. This leads to a finite SOC[30, 31], which lifts the degeneracy in the conduction band and gives rise to two spin-orbit-split sub-bands in each valley[16, 30]. When combined to the gate-induced SC state[31], this can give rise to interesting physics, such as spin-valley locking of the Cooper pairs[32] and 2d Ising superconductivity (SC)[33], suggested to host topologically non-trivial SC states[40, 42, 43]. Refs.16, 19 predicted SOC and spin-orbit splitting between sub-bands to be significantly stronger for the Q/Q' valleys than for K/K', thus supporting spin-valley locking at Q/Q' as well[44]. From the experimental point of view, the possible multi-valley character of transport in gated TMDs is currently debated. Refs.44–46 measured the Landau-level degeneracy at moderate carrier densities ($n_{2d} \sim 10^{12} - 10^{13}\text{cm}^{-2}$), finding it compatible with a carrier population in the Q/Q' valleys. However, Ref.46 argued that this feature would be suppressed for larger doping levels ($n_{2d} \gtrsim 10^{13}\text{cm}^{-2}$, typical of ion-gated devices and mandatory for the emergence of SC) due to stronger confinement within the first layer[46]. In contrast, angle-resolved photoemission spectroscopy in surface-Rb-doped TMDs[39] highlighted the presence of a non-negligible spectral weight at the Q/Q' valleys only for $n_{2d} \gtrsim 8 \cdot 10^{13}\text{cm}^{-2}$ in the case of MoS_2. Thus, which valleys and sub-bands are involved in the gate-induced SC state at the surface of MoS_2 still demands a satisfactory answer.

Here we report multi-valley transport and SC at the surface of liquid-gated FL-MoS_2. We use a dual-gate geometry to tune doping across a wide range of carrier densities ($n_{2d} \simeq 5 \cdot 10^{12} - 1 \cdot 10^{14}\text{cm}^{-2}$), induce SC, and detect characteristic "kinks" in the transconductance. These are non-monotonic features that emerge in the n_{2d}-dependence of the low-temperature (T) conductivity when E_F crosses the high-energy sub-bands[35]. We show that the population of the Q/Q' valleys is fundamental for the emergence of SC. The crossing of the first sub-band Q_1 (Fig.1c) occurs at small carrier densities ($n_{2d} \lesssim 2 \cdot 10^{13}\text{cm}^{-2}$), implying that multi-valley transport already occurs in the metallic phase over a wide range of doping ($n_{2d} \simeq 2 - 6 \cdot 10^{13}\text{cm}^{-2}$). We also show that the crossing of the second sub-band Q_2 occurs after a finite T_c is observed, while a full population of both spin-orbit-split sub-bands (Fig.1d) in the Q/Q' valleys is required to reach the maximum T_c. These results highlight how SC can be enhanced in MoS_2 by optimizing the connectivity of its Fermi Surface (FS), i.e. by adding extra FSs in different BZ regions to provide coupling to further phonon branches[47].

Since the evolution of the band structure of MoS_2 with field-effect doping is analogous to that of other semiconducting TMDs[16, 35, 39, 41, 44], a similar mechanism is likely associated to the emergence of SC in TMDs in general. Thus, optimization of the FS connectivity can be a viable strategy in the search of new superconductors.

RESULTS

Device fabrication and characterization

We study flakes with N between 4 and 10, as Refs.4, 16, 35 predicted that FL flakes with 4 or more layers are representative of the bulk electronic structure, and Ref.34 experimentally observed that both T_c and the critical magnetic field B_c in 4L flakes are similar to those of 6L and bulk flakes. Our devices are thus comparable with those in literature[23, 32–34, 38]. We do not consider 1L flakes as they exhibit a lower T_c and their mobility is suppressed due to disorder[34, 38].

FL-MoS_2 flakes are prepared by micro-mechanical cleavage[36] of 2H-MoS_2 crystals from SPI Supplies. The 2H phase is selected to match that in previous reports of gate-induced SC[23, 34]. Low resistivity ($< 0.005\Omega\cdot$cm) Si coated with a thermal oxide SiO_2 is chosen as a substrate. We tested both 90 or 285nm SiO_2 obtaining iden-

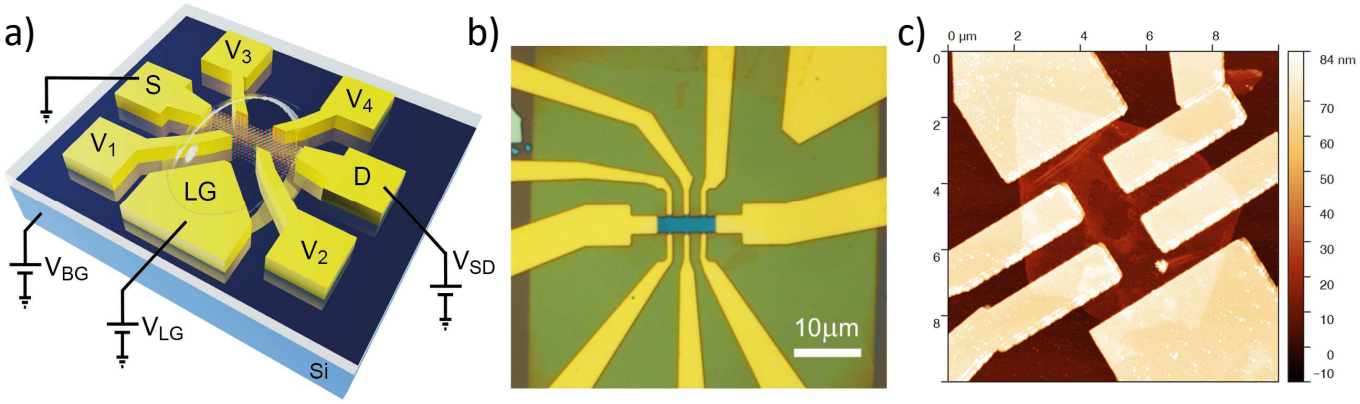

FIG. 2: a) Hall bar FL-MoS_2 flake with voltage probes (V_i), source (S), drain (D) and liquid-gate (LG) electrodes. A droplet of ionic liquid covers the flake and part of the LG electrode. The sample is biased with a source-drain voltage (V_{SD}) and dual gate control is enabled by a voltage applied on the liquid gate (V_{LG}) and on the solid back gate (V_{BG}). b) Optical image of a patterned Hall bar with six voltage probes. The LG electrode is on the upper-right corner. c) AFM scan of the MoS_2 Hall bar after ionic liquid removal.

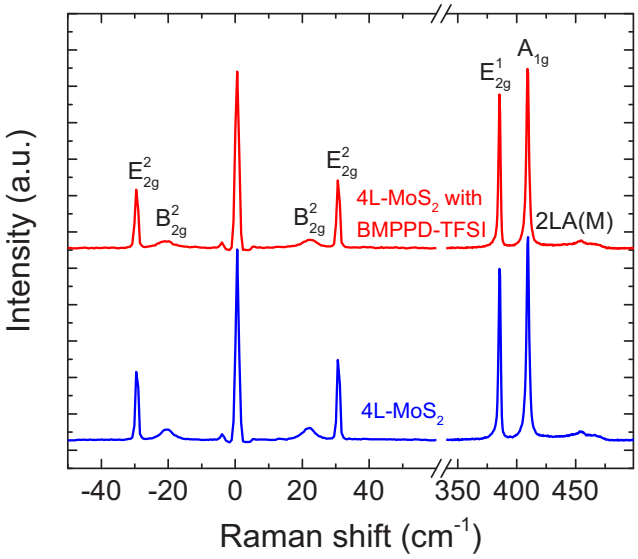

FIG. 3: Representative Raman spectra at 514nm of a 4L-MoS_2 flake before (blue curve) and after (red curve) device fabrication, deposition of the ionic liquid droplet and low-T transport measurements.

tical SC results. Thus, 90nm SiO_2 is used to minimize the back gate voltage V_{BG} (-30V< V_{BG} <30V), while 285nm is used to minimize leakage currents through the back gate I_{BG}. Both SiO_2 thicknesses provide optical contrast at visible wavelengths[49]. A combination of optical contrast, Raman spectroscopy and atomic force microscopy (AFM) is used to select the flakes and determine N.

Electrodes are then defined by patterning the contacts area by e-beam lithography, followed by Ti:10nm/Au:50nm evaporation and lift-off. Ti is used as an adhesion layer[77], while the thicker Au layer provides the electrical contact. Flakes with irregular shapes are further patterned in the shape of Hall bars by using polymethyl methacrylate (PMMA) as a mask and removing the unprotected MoS_2 with reactive ion etching (RIE) in a 150mTorr atmosphere of CF_4:O_2=5:1, as shown in Figs.2a,b. A droplet of 1-Butyl-1-methylpiperidinium bis(trifluoromethylsulfonyl)imide (BMPPD-TFSI) is used to cover the FL-MoS_2 surface and part of the side electrode for liquid gate operation (LG), as sketched in Fig.2a.

AFM analysis is performed with a Bruker Dimension Icon in tapping mode. The scan in Fig.2c is done after the low-T experiments and removal of the ionic liquid, and confirms that the FL-MoS_2 sample does not show topographic damage after the measurement cycle.

We use Raman spectroscopy to characterize the devices both before and after fabrication and BMPPD-TFSI deposition. Raman measurements are performed with a Horiba LabRAM Evolution at 514nm, with a 1800grooves/mm grating and a spectral resolution$\sim$0.45cm^{-1}. The power is kept below 300μW to avoid any damage. A representative Raman spectrum of 4L-MoS_2 is shown in Fig.3 (blue curve). The peak at$\sim$455cm^{-1} is due to a second-order longitudinal acoustic mode at the M point[53]. The E^1_{2g} peak at$\sim$385cm^{-1} and the A_{1g} at$\sim$409cm^{-1} correspond to in-plane and out-of plane vibrations of Mo and S atoms[50, 51]. Their difference, Pos(E^1_{2g})-Pos(A_{1g}), is often used to monitor N[52]. However, for N$\geq$4, the variation in Pos(E^1_{2g})-Pos(A_{1g}) between N and N+1 approaches the instrument resolution[52] and this method is no longer reliable. Thus, we use the low frequency modes (< 100cm^{-1}) to monitor N[54, 56]. The shear (C) and layer breathing modes (LBM) are due to the relative motions of the atomic planes, either perpendicular or parallel to their normal[54]. Pos(C) and Pos(LBM) change with N ac-

cording to[54, 56]:

$$\mathrm{Pos(C)_N} = \frac{1}{\sqrt{2}\pi c}\sqrt{\frac{\alpha_\parallel}{\mu_m}}\sqrt{1+\cos\left(\frac{\pi}{N}\right)} \qquad (1)$$

$$\mathrm{Pos(LBM)_N} = \frac{1}{\sqrt{2}\pi c}\sqrt{\frac{\alpha_\perp}{\mu_m}}\sqrt{1-\cos\left(\frac{\pi}{N}\right)} \qquad (2)$$

where $\alpha_\parallel \sim 2.82{\cdot}10^{19}\mathrm{N/m^3}$ and $\alpha_\perp \sim 8.90{\cdot}10^{19}\mathrm{N/m^3}$ are spring constants for C and LBM modes, respectively, c is the speed of light in vacuum, $\mu_m \sim 3{\cdot}10^{-6}\mathrm{Kg/m^2}$ is the 1L mass per unit area[54, 56]. Fig.3 shows a C mode at$\sim$30cm^{-1} and an LBM at$\sim$22cm^{-1}. These correspond to N=4 using Eqs.1,2. Fig.3 also plots the Raman measurements after device fabrication, deposition of the ionic liquid, low-T measurements, V_{LG} removal and warm-up to room T (red curve). We still find Pos(C)$\sim$30cm^{-1} and Pos(LBM)$\sim$22cm^{-1}, the same as those of the pristine flake, suggesting no damage nor residual doping.

Transport measurements

Four-probe resistance and Hall measurements are then performed in the vacuum chambers of either a Cryomech pulse-tube cryocooler, T_{min}=2.7K, or a Lakeshore cryogenic probe-station, T_{min}=8K, equipped with a 2T superconducting magnet. A small ($\sim 1\mu$A) constant current is applied between S and D contacts (see Fig.2a) by using a two-channel Agilent B2912A source-measure unit (SMU). The longitudinal and transverse voltage drops are measured with an Agilent 34420 low-noise nanovoltmeter. Thermoelectrical and other offset voltages are eliminated by measuring each resistance value inverting the source current in each measurement[74]. Gate biases are applied between the corresponding G electrode and D contact with the same two-channel SMU (liquid gate) or a Keithley 2410 SMU (back gate). Samples are allowed to degas in high vacuum ($< 10^{-5}$mbar) at room T for at least$\sim$ 1h before measurements, in order to remove residual water traces in the electrolyte.

We first characterize the T dependence of the sheet resistance, R_s, under the effect of the liquid top gate. We apply the liquid gate voltage, V_{LG}, at 240K, where the electrolyte is still liquid, and under high-vacuum ($< 10^{-5}$mbar) to minimize unwanted electrochemical interactions and extend the stability window of the ionic liquid[21]. After V_{LG} is applied, we allow the ion dynamics to settle for$\sim$10min before cooling to a base T=2.7K.

Fig.4a plots the T dependence of R_s measured in a four-probe configuration, for different V_{LG} and induced carrier density n_{2d}. Our devices behave similarly to Ref.23, undergoing first an insulator-to-metal transition near $R_s \simeq h/e^2$ at low carrier densities ($n_{2d} < 1\cdot 10^{13}\mathrm{cm^{-2}}$), followed by a metal-to-superconductor transition at high carrier densities ($n_{2d} > 6\cdot 10^{13}\mathrm{cm^{-2}}$). We employ Hall effect measurements to determine n_{2d} as a function of V_{LG} (see Fig.4b), and, consequently, the liquid gate capacitance C_{LG}. We find that C_{LG} for the BMPPD-TFSI/MoS_2 interface ($\sim 3.4 \pm 0.6\mu\mathrm{F/cm^2}$) is of the same order of magnitude as that for the DEME-TFSI/MoS_2 of Ref.57 ($\sim 8.6 \pm 4.1\mu\mathrm{F/cm^2}$), where DEME-TFSI is the N,N-Diethyl-N-methyl-N-(2-methoxyethyl)ammonium bis(trifluoromethanesulfonyl)imide ionic liquid[57].

Fig.4a shows that, while for T$\gtrsim$100K R_s is a monotonically decreasing function of n_{2d}, the same does not hold for T$\lesssim$100K, where the various curves cross. In particular, the residual R_s in the normal state R_s^0 (measured just above T_c when the flake is superconducting) varies non-monotonically as a function of n_{2d}. This implies the existence of multiple local maxima in the $R_s^0(n_{2d})$ curve. Consistently with the theoretical predictions of Ref.35, we find two local maxima (see Fig.5e). The first and more pronounced occurs when the flake is superconducting, i.e. for $n_{2d} > 6\cdot 10^{13}\mathrm{cm^{-2}}$. This feature was also reported in Refs.23, 33, but not discussed. The second, less pronounced kink, is observed for $1{\cdot}10^{13} \lesssim n_{2d} \lesssim 2{\cdot}10^{13}\mathrm{cm^{-2}}$, not previously shown. Both kinks can be clearly seen only for T$\lesssim$70K and they are smeared out for T$\gtrsim$150K.

The kink that emerges in correspondence of the superconducting dome extends across a wide range of V_{LG} ($3 \lesssim V_{LG} \lesssim 6$V) for $n_{2d} \gtrsim 6\cdot 10^{13}\mathrm{cm^{-2}}$, and can be accessed only by LG biasing due to the small capacitance of the solid BG. This prevents a continuous characterization of its behavior, as the n_{2d} induced by the LG cannot be altered for $T \lesssim 220$K as the ions are locked in place when the electrolyte is frozen. The kink that appears early in the metallic state, on the other hand, extends across a small range of n_{2d} ($1 \lesssim n_{2d} \lesssim 2\cdot 10^{13}\mathrm{cm^{-2}}$), and is ideally suited to be explored continuously by exploiting the dual-gate configuration.

We thus bias our samples in the low-density range of the metallic state ($n_{2d} \simeq 7\cdot 10^{12}\mathrm{cm^{-2}}$) by applying $\mathrm{V}_{LG} = 0.9$V, and cool the system to 2.7K. We then apply V_{BG} and fine-tune n_{2d} across the kink. We constantly monitor I_{BG} to avoid dielectric breakdown. Fig.4c plots the transconductance σ_{2d} response of a representative device to multiple V_{BG} sweeps, as n_{2d} is tuned across the kink. The device reproduces well the behavior observed for low V_{LG} ($1 \lesssim n_{2d} \lesssim 2\cdot 10^{13}\mathrm{cm^{-2}}$). The hysteresis between increasing and decreasing V_{BG} ramps is minimal. This back-gated kink is suppressed by increasing T, similar to LG gating.

V_{BG} provides us an independent tool to estimate n_{2d}: If V_{LG} is small enough ($V_{LG} \lesssim 1$V) so that conduction in the channel can be switched off by sufficiently large negative V_{BG} ($V_{BG} \lesssim -25$V), we can write $n_{2d} = C_{ox}/e\cdot(V_{BG}-V_{th})$. Here, $C_{ox} = \epsilon_{ox}/d_{ox}$ is the back gate oxide specific capacitance, $e = 1.602\cdot 10^{-19}$C is the elementary charge and V_{th} is the threshold voltage required to observe a finite conductivity in the de-

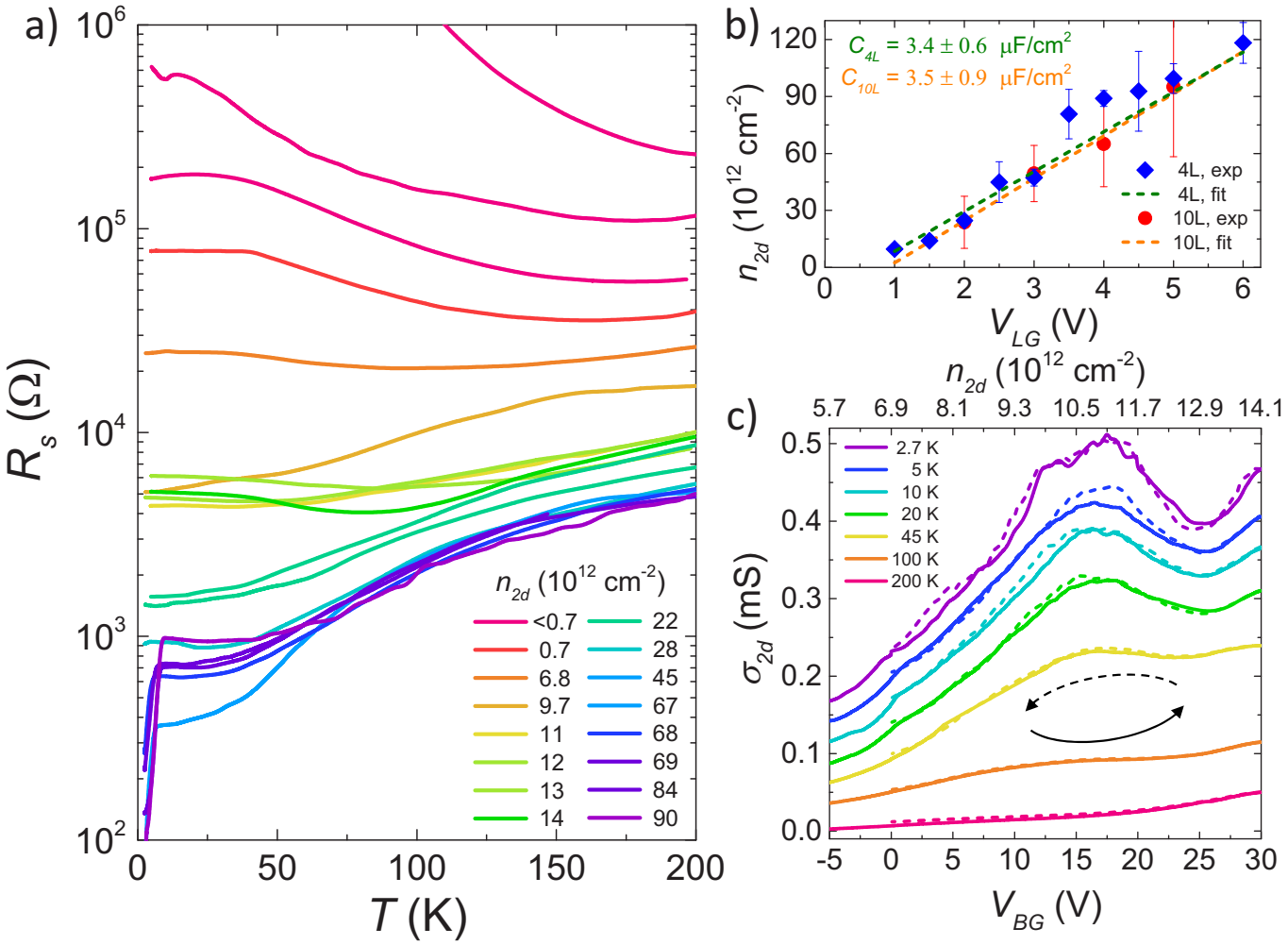

FIG. 4: Transport of dual-gated 4L-MoS_2. a) R_s as a function of T for different n_{2d}. b) n_{2d} as function of V_{LG} as determined via Hall effect measurements, for N=4 and 10. The liquid gate capacitances are obtained by a linear fit of the data. c) σ_{2d} as a function of V_{BG} at $V_{LG} = 0.9$V, for different T. Each curve is shifted by a constant offset 3.333×10^{-5}S. The top scale shows the values of n_{2d} estimated from C_{ox}. Solid (dashed) curves are measured for increasing (decreasing) V_{BG}.

vice. We neglect the quantum capacitance C_q of MoS_2, since $C_q \gtrsim 100\mu$F/cm$^2 \gg C_{ox}$[16]. By using the dielectric constant of SiO_2 ϵ_{ox}=3.9[75] and an oxide thickness t_{ox} = 90nm (or t_{ox} = 285nm, depending on the experiment) we obtain the n_{2d} scale in the top axis of Fig.4c, in good agreement with the corresponding values in Fig.4a, estimated from the Hall effect measurements in Fig.4b.

DISCUSSION

The bandstructure of field-effect doped NL-MoS_2 (Figs.1b-d) depends on N[16] and strain[35]. A fully relaxed N-layer flake, with N≥3, has been predicted to behave as follows[16, 35]: For small doping ($x \lesssim 0.05$e$^-$/unit cell, Fig.1b) only the two spin-orbit split sub-bands at K/K' are populated. At intermediate doping ($0.05 \lesssim x \lesssim 0.1$ e$^-$/unit cell, Fig.1c), E_F crosses the first spin-orbit split sub-band at Q/Q' (labeled Q_1). For large doping ($x \gtrsim 0.1$ e$^-$/unit cell, Fig.1d) E_F crosses the second sub-band (Q_2) and both valleys become fully populated[16]. Even larger doping ($x \gtrsim 0.35$ e$^-$/unit cell) eventually shifts the K/K' valleys above E_F[16].

When E_F crosses these high-energy sub-bands at Q/Q', sharp kinks are expected to appear in the transconductance of gated FL-MoS_2[35]. These are reminiscent of a similar behavior in liquid-gated FL graphene[59–61]. Ref.35 showed that the in-plane conductivity σ_{2d} can be expressed as:

$$\sigma_{2d} = e^2 \tau \langle v_\parallel^2 \rangle N(E_F) \propto e^2 \langle v_\parallel^2 \rangle \quad (3)$$

where τ is the average scattering time, and $N(E_F)$ is the density of states (DOS) at E_F. This implies that σ_{2d} is proportional to the average of the squared in-plane velocity $\langle v_\parallel^2 \rangle$ over the FS[35]. For a quadratic dispersion in 2d, the DOS is expected to be constant with the ap-

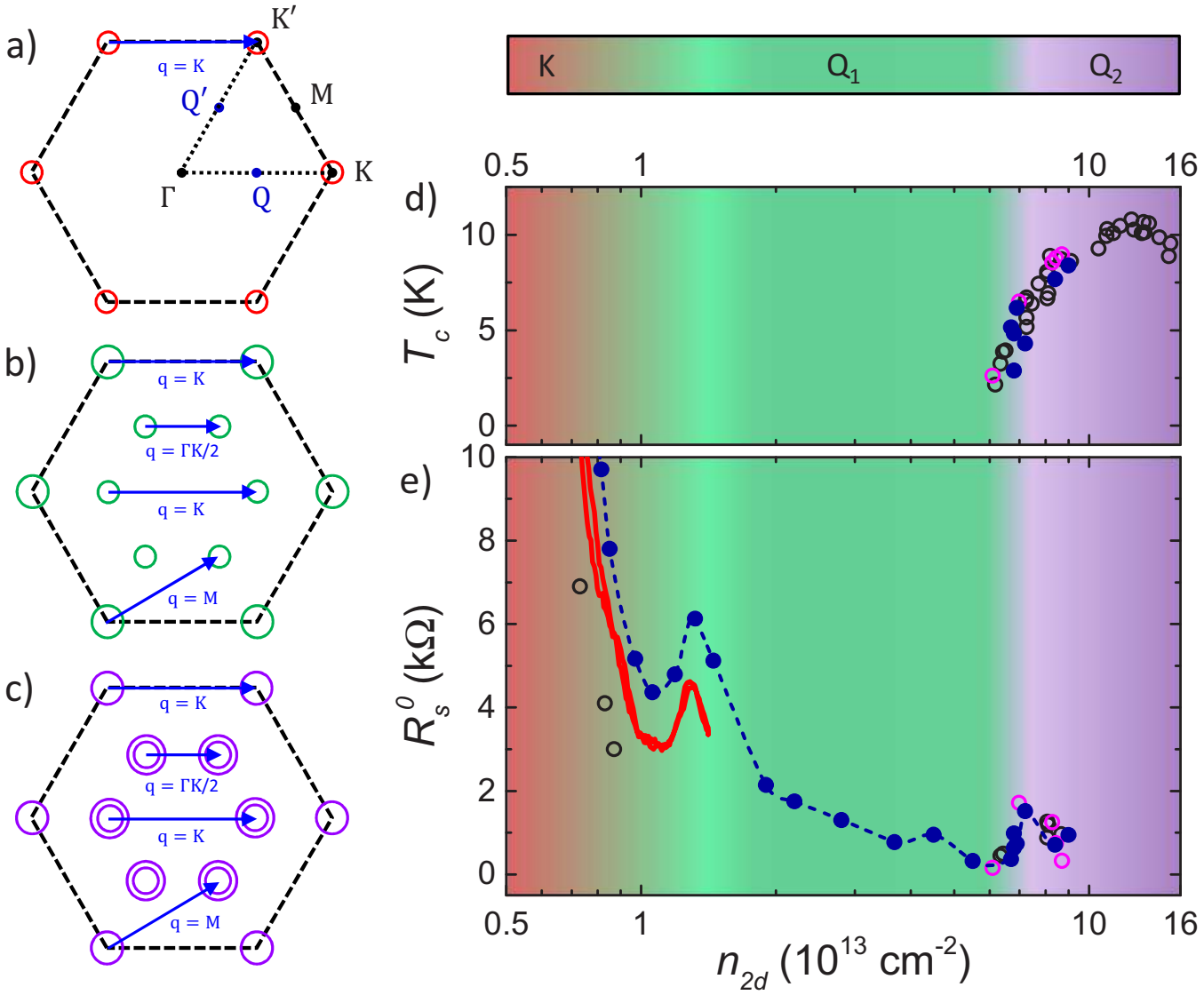

FIG. 5: a-c) Fermi Surface of 3L-MoS_2 for the 3 doping values in Fig.1b-d. High symmetry points Γ, M, K, K', and points Q and Q' are highlighted. Blue arrows indicate representative phonon wave vectors that connect the various FSs. d) SC dome of liquid-gated MoS_2 as a function of n_{2d}. T_c is determined at 90% of the total transition. e) R_s^0 as a function of n_{2d}, for increasing V_{LG} (blue filled circles) and V_{BG} (solid red line). In d,e), filled circles are data measured here, black and magenta open circles are taken from Refs.23, 33. The background is color-coded to indicate the doping ranges highlighted in panels a-c).

pearance of steps when E_F crosses a new band[35]. $\langle v_{\parallel}^2 \rangle$ linearly increases with increasing n_{2d} and drops sharply as soon as a new band starts to get doped[35]. Therefore, kinks observed in σ_{2d} (or, equivalently, R_s) at $T \lesssim 15$K can be used to determine the onset of doping of the sub-bands in the Q/Q' valleys. Additionally, their presence is predicted to be suppressed by increasing T[35].

We show evidence for such a behavior in Fig.5e, where we plot R_s^0 as a function of n_{2d}. The electric field is applied both in liquid-top-gate (filled dots and dashed line) and dual-gate (solid red line) configurations. For comparable values of n_{2d}, the liquid-gate geometry features larger R_s^0 than in back-gated. This difference is due to increased disorder introduced when n_{2d} is modulated via ionic gating[60–62, 66, 67]. Two kinks appear in the n_{2d} dependence of R_s: a low-doping one for $1.5 \cdot 10^{13} \lesssim n_{2d} \lesssim 2 \cdot 10^{13}\text{cm}^{-2}$, and a high-doping one for $7 \cdot 10^{13} \lesssim n_{2d} \lesssim 9 \cdot 10^{13}\text{cm}^{-2}$. A plot of the SC dome of gated MoS_2 on the same n_{2d} scale (Fig.5d), shows that the low-doping kink appears well before the onset of the SC state, while the second kink appears immediately after, before the maximum T_c is reached.

These results can be interpreted as follows. When $n_{2d} \lesssim 1 \cdot 10^{13}\text{cm}^{-2}$, only the spin-orbit split sub-bands at K/K' are populated, and the FS is composed only by two pockets, Fig.5a. For n_{2d} between$\sim$ 1.5 and

$2 \cdot 10^{13}$cm^{-2}, E_F crosses the bottom of the Q_1 sub-band and two extra pockets appear in the FS at Q/Q'[16, 18], Fig.5b. The emergence of these pockets induces a Lifshitz transition, i.e. an abrupt change in the topology of the FS[68]. Once Q_1 is populated and E_F is large enough ($n_{2d} \sim 6 \cdot 10^{13}$cm^{-2}), the system becomes superconducting[23, 33]. For slightly larger E_F ($7 \cdot 10^{13} \lesssim n_{2d} \lesssim 9 \cdot 10^{13}$cm^{-2}), E_F crosses the bottom of Q_2 resulting in a second Lifshitz transition, and other two pockets emerge in the FS at Q/Q'[16], Fig.5c.

We note that the experimentally observed kinks are at different n_{2d} with respect to the theoretically ones for 3L-MoS_2[35]. Ref.35 predicted that for a 1.28% in-plane tensile strain, Q_1 and Q_2 should be crossed for $n_{2d} \sim 5{\cdot}10^{13}$ and $\sim 1{\cdot}10^{14}$. Since the positions of the sub-band crossings are strongly dependent on strain[35], we estimate the strain in our devices by monitoring the frequency of the E^1_{2g} mode[78, 79] via Raman spectroscopy. Strain can arise due to a mismatch in the thermal expansion coefficients (TECs) of MoS_2[80], SiO_2 substrate[81] and Au electrodes[82]. Upon cooling, MoS_2, SiO_2 and Au would normally undergo a contraction. However the MoS_2 flake is also subjected to a tensile strain due to TEC mismatch[78]. The amount of strain ϵ_{MoS_2} due to the MoS_2-SiO_2 TEC mismatch is:

$$\epsilon_{MoS_2} = \int_T^{292K} [\alpha_{MoS_2}(T) - \alpha_{SiO_2}(T)]dT \qquad (4)$$

whereas the strain ϵ_{Au} due to the Au contacts is:

$$\epsilon_{Au} = \int_T^{292K} [\alpha_{Au}(T) - \alpha_{SiO_2}(T)]dT \qquad (5)$$

ϵ_{MoS_2} and ϵ_{Au} are$\sim$0.1% and$\sim$0.3% at $\sim$4K, respectively[78]. Any FL-MoS_2 flake on SiO_2 will be subject to ϵ_{MoS_2} at low T. When the flake is contacted, an additional contribution is present due to ϵ_{Au}. This can be more reliably estimated performing T-dependent Raman scattering and comparing the Raman spectra for contacted and un-contacted flakes[78, 79]. Figs.6a,b show how a T decrease results in the E^1_{2g} mode shifting to higher frequencies for both as-prepared and contacted 4L-MoS_2, due to anharmonicity[83]. However, in the as-prepared 4L-MoS_2, the up-shift is$\sim$1cm^{-1} larger with respect to the contacted one. This difference points to a further tensile strain. Refs.84, 85 suggested that uniaxial tensile strain on 1L-MoS_2 induces a E^1_{2g} softening and a splitting in two components: $E^1_{2g}(+)$ and $E^1_{2g}(-)$[84, 85]. The shift rates for $E^1_{2g}(+)$ and $E^1_{2g}(-)$ are from -0.9 to -1.0cm^{-1}/% and from -4.0 to -4.5cm^{-1}/%, respectively[84, 85]. We do not observe splitting, pointing towards a biaxial strain. As for Ref.79, we calculate a shift rate of the E^1_{2g} mode for biaxial strain from -7.2 to -8.2cm^{-1}/%. The amount of tensile strain on the 4L-MoS_2 device can thus be estimated. The E^1_{2g} mode up-shift difference between

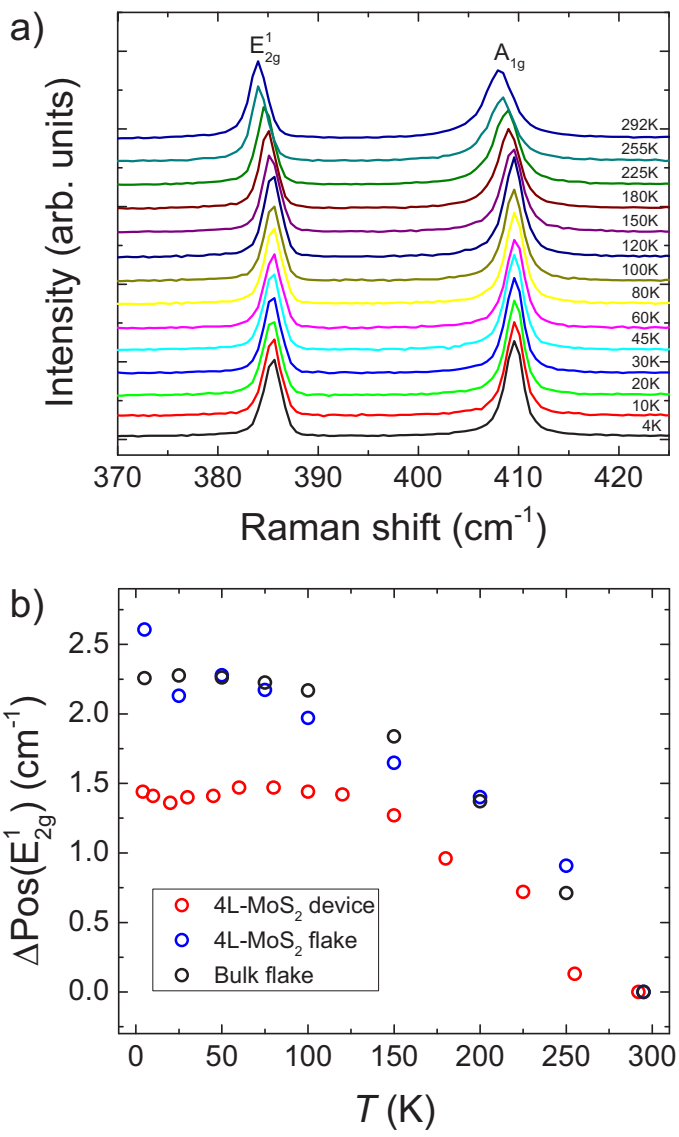

FIG. 6: a) Raman spectra of the 4L-MoS_2 device in Fig.2c from 4 to 292K. b) Shift in the position of the E^1_{2g} mode as a function of T in an as-prepared 4L-MoS_2 flake (blue circles) and a 4L-MoS_2 device with Au contacts.

the contacted and as-prepared 4L-MoS_2, ΔPos(E^1_{2g}), at 4K is$\sim$-1.0cm^{-1}, corresponding to an additional $\sim$0.13% biaxial tensile strain. Thus, assuming a 0.1% strain for the as-prepared 4L-MoS_2 due to TEC mismatch with SiO_2, we estimate the total strain in the contacted 4L-MoS_2 to be$\sim$0.23% at$\sim$4K.

Fig.7a shows that, for 0.23% tensile strain, the experimentally observed positions of the kinks agree well with a linear extrapolation of the data of Ref.35 to 4L-MoS_2 (representative of our experiments) and for in-plane strain between 0% (bulk) and 1.28% (fully relaxed). These findings indicate that, while the mechanism proposed in Ref.18 qualitatively describes the general behavior of gated FL-MoS_2, quantitative differences arise

due to the spin-orbit split of the Q_1 and Q_2 sub-bands. The main reason for the EPC (and, hence, T_c) increase is the same, i.e. the increase in the number of phonon branches involved in the coupling when the high-energy valleys are populated[18]. However, the finite spin-orbit-split between the sub-bands significantly alters the FS connectivity upon increasing doping[16]. If we consider the relevant phonon wave vectors (q=Γ,K,M,ΓK/2) for 1L- and FL-MoS_2[70, 71], and only the K/K' valleys populated, then only phonons near Γ and K can contribute to EPC[18]. The former strongly couple electrons within the same valley[18], but cannot contribute significantly due to the limited size of the Fermi sheets[18]. The latter couple electrons across different valleys[18], and provide a larger contribution[18], insufficient to induce SC. MoS_2 flakes are metallic but not superconducting before the crossing of Q_1. When this crossing happens, the total EPC increases due to the contribution of longitudinal phonon modes near K[18] (coupling states near two different Q or Q'), near ΓK/2[18] (coupling states near Q to states near Q'), and near M[18] (coupling states near Q or Q' to states near K or K'). However, this first EPC increase associated to Q_1 is not sufficient to induce SC, as the SC transition is not observed until immediately before the crossing of the spin-orbit-split sub-band Q_2 and the second doping-induced Lifshitz transition. Additionally, the SC dome shows a maximum in the increase of T_c with doping (dT_c/dn_{2d}) across the Q_2 crossing, i.e. when a new Fermi sheet emerges. Consistently, the subsequent reduction of T_c for $n_{2d} \geq 13 \cdot 10^{13}\text{cm}^{-2}$ can be associated to the shrinkage and eventual disappearance of the Fermi sheet at K/K'[16, 18], and might also be promoted by the formation of an incipient Charge Density Wave[48] (i.e. a phase characterized by periodic modulations of the carrier density coupled to a distortion of the lattice structure[76]).

Since the evolution of the bandstructure with doping is similar in several semiconducting TMDs[16, 35, 39, 41, 44], this mechanism is likely not restricted to gated MoS_2. The sharp increase in T_c in correspondence to a Lifshitz transition is reminiscent of a similar behavior observed in $CaFe_2As_2$ under pressure[72], suggesting that the mechanism highlighted here may be a general feature across different classes of materials.

We note that the maximum $T_c \sim 11$K is reached at $n_{2d} \simeq 12 \cdot 10^{13}\text{cm}^{-2}$, shortly after the closing of the second kink. This indicates that the population of the Q_2 sub-band close to the second Lifshitz transition is a critical requirement for the T_c enhancement in the first half of the SC dome. We address this quantitatively with the Allen-Dynes formula[73], which describes the dependence of T_c by a numerical approximation of the Eliashberg theory accurate for materials with a total $\lambda \lesssim 1.5$[73]:

$$T_c(n_{2d}) = \frac{\omega_{ln}}{1.2}\exp\left\{\frac{-1.04\,[1+\lambda(n_{2d})]}{\lambda(n_{2d}) - \mu^*\,[1+0.62\lambda(n_{2d})]}\right\} \quad (6)$$

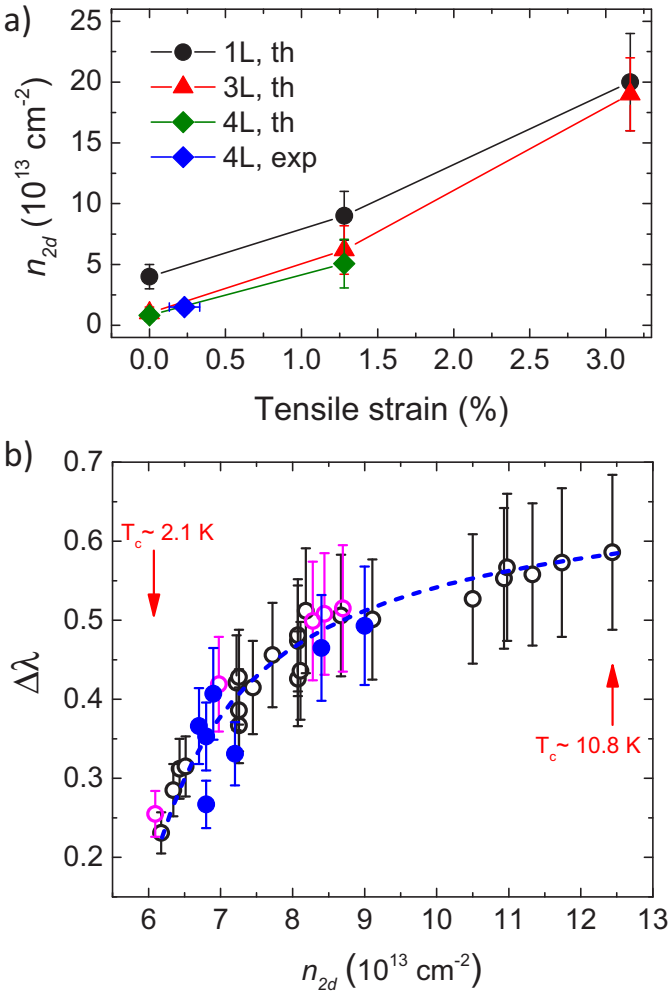

FIG. 7: a) Surface carrier densities required to cross the Q_1 sub-band in FL-MoS_2 as a function of tensile strain. Theoretical values for 1L (black dots and line) and 3L (red triangle and line) from Ref.35; values for 4L (green diamonds and line) are by linear extrapolation. Blue diamond is the present experiment. b) EPC enhancement due to the crossing of the Q_2 sub-band, $\Delta\lambda$, as a function of n_{2d}, assuming $\omega_{ln} = 230 \pm 30$K and $\mu^* = 0.13$[18]. Filled blue circles are our experiments. Black and magenta open circles from Refs.23, 33. The blue dashed line is a guide to the eye.

where $\lambda(n_{2d})$ is the total EPC as a function of doping, ω_{ln} is the representative phonon frequency and μ^* is the Coulomb pseudo-potential. If we consider the difference between the experimental $T_c(n_{2d})$ and that immediately before the approach and crossing of the sub-band at Q_2, $T_{c,min}$, we can obtain the EPC increase $\Delta\lambda = \lambda(n_{2d}) - \lambda_{min}$, i.e., the fraction of the total EPC due to the gradual appearance of electron pockets at Q_2. By setting $\omega_{ln} = 230 \pm 30$K and $\mu^* = 0.13$ (as for Ref.18), $T_{c,min} = 15 \pm 5$mK at n_{2d} slightly lower than $6 \cdot 10^{13}\text{cm}^{-2}$, this gives $\lambda_{min} \sim 0.3$ and the $\Delta\lambda$ vs. n_{2d} dependence in Fig.7b. The crossing at Q_2 results in a maximum $\Delta\lambda/\lambda_{min} = 1.8 \div 2.1$, i.e. a $\sim 300\%$ enhance-

ment. This indicates that the largest contribution to the total EPC, hence to the maximum $T_c \sim 11$K, is associated with the population of the Q_2 sub-band. This is consistent with the reports of a reduced $T_c \sim 2$K in 1L-MoS_2[34, 38], shown to be SC for smaller carrier densities ($n_{2d} \simeq 5.5 \cdot 10^{13}$cm^{-2})[38], hence likely to populate the Q_1 sub-band only. $n_{2d} \sim 5 \cdot 10^{13}$cm^{-2} is also the doping expected for the crossing of the Q_1 sub-band in 1L-MoS_2 in presence of a low-T strain similar to that in our 4L-MoS_2 devices (see Fig.7a).

CONCLUSIONS

We exploited the large carrier density modulation provided by ionic gating to explore sub-band population and multivalley transport in MoS_2 layers. We detected two kinks in the conductivity, associated to the doping-induced crossing of the two sub-bands at Q/Q'. By comparing the emergence of these kinks with the doping dependence of T_c, we showed how superconductivity emerges in gated MoS_2 when the Q/Q' valleys are populated, while previous works only considered the filling of K/K'. We highlighted the critical role of the population of the second spin-orbit-split sub-band, Q_2, (and the consequent increase of the FS available for EPC) in the appearance of superconductivity and in the large enhancement of T_c and of EPC in the first half of the superconducting dome. Our findings explain the doping dependence of the SC state at the surface of gated FL-MoS_2, and provide a key insight for other semiconducting transition metal dichalcogenides.

ACKNOWLEDGMENTS

We thank M. Calandra for useful discussions. We acknowledge funding from EU Graphene Flagship, ERC Grant Hetero2D, EPSRC Grant Nos. EP/509K01711X/1, EP/K017144/1, EP/N010345/1, EP/M507799/ 5101, and EP/L016087/1 and the Joint Project for the Internationalization of Research 2015 by Politecnico di Torino and Compagnia di San Paolo.

* These authors contributed equally to this work.
† Electronic address: renato.gonnelli@polito.it

[1] A. C. Ferrari, F. Bonaccorso, V. Fal'ko, K. S. Novoselov, S. Roche, P. Boggild, S. Borini, F. H. L. Koppens, V. Palermo, N. Pugno, J. A. Garrido, R. Sordan, A. Bianco, L. Ballerini, M. Prato, E. Lidorikis, J. Kivioja, C. Marinelli, T. Ryhanen, A. Morpurgo *et al.*, Science and technology roadmap for graphene, related two-dimensional crystals, and hybrid systems. *Nanoscale* **7**, 4598 (2015).

[2] Q. H. Wang, K. Kalantar-Zadeh, A. Kis, J. N. Coleman and M. S. Strano, Electronics and optoelectronics of two-dimensional transition metal dichalcogenides. *Nat. Nanotechnol.* **7**, 699 (2012)

[3] K. F. Mak, C. Lee, J. Hone, J. Shan and T. F. Heinz, Atomically thin MoS_2: a new direct-gap semiconductor. *Phys. Rev. Lett.* **105**, 136805 (2010)

[4] A. Splendiani, L. Sun, Y. B. Zhang, T. S. Li, J. Kim, C. Y. Chim, G. Galli and F. Wang, Emerging photoluminescence in monolayer MoS_2. *Nano Lett.* **10**, 1271 (2010)

[5] K. F. Mak and J. Shan, Photonics and optoelectronics of 2d semiconductor transition metal dichalcogenides. *Nat. Photonics* **10**, 216 (2016)

[6] V. Podzorov, M. E. Gershenson, C. Kloc, R. Zeis and E. Bucher, High-mobility field-effect transistors based on transition metal dichalcogenides. *Appl. Phys. Lett.* **84**, 3301 (2004)

[7] B. Radisavljevic, A. Radenovic, J. Brivio, V. Giacometti and A. Kis, Single-layer MoS_2 transistors. *Nat. Nanotechnol.* **6**, 147 (2011)

[8] H. Fang, S. Chuang, T. C. Chang, K. Takei, T. Takahashi and A. Javey, High-Performance Single Layered WSe_2 p-FETs with Chemically Doped Contacts. *Nano Lett.* **12**, 3788 (2012)

[9] E. Gourmelon, O. Lignier, H. Hadouda, G. Couturier, J. C. Bernede, J. Tedd, J. Pouzet and J. Salardenne, MS_2 (M=W, Mo) Photosensitive thin films for solar cells. *Sol. Energ. Mat. Sol. Cells* **46**, 115 (1997)

[10] H. S. Lee, S. W. Min, Y. G. Chang, M. K. Park, T. Nam, H. Kim, J. H. Kim, S. Ryu and S. Im, MoS_2 Nanosheet Phototransistors with Thickness-Modulated Optical Energy Gap. *Nano Lett.* **12**, 3695 (2012)

[11] Z. Y. Yin, H. Li, H. Li, L. Jiang, Y. M. Shi, Y. H. Sun, G. Lu, Q. Zhang, X. D. Chen and H. Zhang, Single-Layer MoS_2 Phototransistors. *ACS Nano* **6**, 74 (2012)

[12] F. H. L. Koppens, T. Mueller, P. Avouris, A. C. Ferrari, M. S. Vitiello and M. Polini, Photodetectors based on graphene, other two-dimensional materials and hybrid systems. *Nat. Nanotechnol.* **9**, 780 (2014).

[13] Z. Sun, A. Martinez and F. Wang, Optical modulators with 2d layered materials. *Nat. Photonics* **10**, 227 (2016)

[14] A. Carladous, R. Coratger, F. Ajustron, G. Seine, R. Pechou and J. Beauvillain, Light emission from spectral analysis of Au/MoS_2 nanocontacts stimulated by scanning tunneling microscopy. *Phys. Rev. B* **66**, (2002)

[15] R. S. Sundaram, M. Engel, A. Lombardo, R. Krupke, A. C. Ferrari, P. Avouris and M. Steiner, Electroluminescence in Single Layer MoS_2. *Nano Lett.* **13**, 1416 (2013)

[16] T. Brumme, M. Calandra, and F. Mauri, First-principles theory of field-effect doping in transition-metal dichalcogenides: Structural properties, electronic structure, Hall coefficient, and electrical conductivity, *Phys. Rev. B* **91**, 155436 (2015)

[17] T. Cheiwchanchamnangij and W. R. L. Lambrecht, Quasiparticle band structure calculation of monolayer, bilayer, and bulk MoS_2, *Phys. Rev. B* **85**, 205302 (2012)

[18] Y. Ge and A. Y. Liu, Phonon-mediated superconductivity in electron-doped single-layer MoS_2: A first-principles prediction, *Phys. Rev. B* **87**, 241408(R) (2013)

[19] E. S. Kadantsev and P. Hawrylak, Electronic structure of a single MoS_2 monolayer, *Solid State Commun.* **152**, 909 (2012)

[20] T. Fujimoto and K. Awaga, Electric-double-layer field-effect transistors with ionic liquids, *Phys. Chem. Chem.*

Phys. **15**, 8983 (2013)
[21] K. Ueno, H. Shimotani, H. T. Yuan, J. T. Ye, M. Kawasaki and Y. Iwasa, Field-induced superconductivity in electric double layer transistors, *J. Phys. Soc. Jpn.* **83**, 032001 (2014)
[22] Y. Saito, T. Nojima, and Y. Iwasa, Gate-induced superconductivity in two-dimensional atomic crystals, *Supercond. Sci. Technol.* **29**, 093001 (2016)
[23] J. T. Ye, Y. J. Zhang, R. Akashi, M. S. Bahramy, R. Arita, and Y. Iwasa, Superconducting dome in a gate-tuned band insulator. *Science* **338**, 1193 (2012)
[24] D. Braga, I. Gutirrez Lezama, H. Berger and A. F. Morpurgo, Quantitative Determination of the Band Gap of WS_2 with Ambipolar Ionic Liquid-Gated Transistors. *Nano Lett.* **12**, 5218 (2012)
[25] Y. Yu, F. Yang, X. F. Lu, Y. J. Yan, H. ChoYong, L. Ma, X. Niu, S. Kim, Y.-W. Son, D. Feng *et al.*, Gate-tunable phase transitions in thin flakes of 1T-TaS_2. *Nat. Nanotechnol.* **10**, 270 (2015)
[26] X. Xi, L. Zhao, Z. Wang, H. Berger, L. Forr, J. Shan and K. F. Mak, Strongly enhanced charge-density-wave order in monolayer $NbSe_2$. *Nat. Nanotechnol.* **10**, 765 (2015)
[27] B. Chakraborty, A. Bera, D. V. S. Muthu, S. Bhowmick, U. V. Waghmare, and A. K. Sood, Symmetry-dependent phonon renormalization in monolayer MoS_2 transistor, *Phys. Rev. B* **85**, 161403 (2012)
[28] A. Das, S. Pisana, B. Chakraborty, S. Piscanec, S. K. Saha, U. V. Waghmare, K. S. Novoselov, H. R. Krishnamurthy, A. K. Geim, A. C. Ferrari, and A. K. Sood, Monitoring dopants by Raman scattering in an electrochemically top-gated graphene transistor, *Nat. Nanotechnol.* **3**, 210 (2008)
[29] A. Das, B. Chakraborty, S. Piscanec, S. Pisana, A. K. Sood, and A. C. Ferrari, Phonon renormalization in doped bilayer graphene, *Phys. Rev. B* **79**, 155417 (2009)
[30] A. Kormányos, Viktor Zólyomi, Neil D. Drummond, Péter Rakyta, Guido Burkard, and Vladimir I. Fal'ko, Monolayer MoS_2: Trigonal warping, the Γ valley, and spin-orbit coupling effects, *Phys. Rev. B* **88**, 045416 (2013)
[31] N. F. Q. Yuan, K. F. Mak, and K.T. Law, Possible Topological Superconducting Phases of MoS_2, *Phys. Rev. Lett.* **113**, 097001 (2014)
[32] Y. Saito, Y. Nakamura, M. S. Bahramy, Y. Kohama, J. T. Ye, Y. Kasahara, Y. Nakagawa, M. Onga, M. Tokunaga, T. Nojima, Y. Yanase, and Y. Iwasa, Superconductivity protected by spin-valley locking in ion-gated MoS_2, *Nat. Phys.* **12**, 14 (2016)
[33] J. M. Lu, O. Zheliuk, I. Leermakers, N. F. Q. Yuan, U. Zeitler, K. T. Law, and J. T. Ye, Evidence for two-dimensional Ising superconductivity in gated MoS_2, *Science* **350**, 1353 (2015)
[34] D. Costanzo, S. Jo, H. Berger, and A. F. Morpurgo, Gate-induced superconductivity in atomically thin MoS_2 crystals, *Nat. Nanotechnol.* **11**, 399 (2016)
[35] T. Brumme, M. Calandra, and F. Mauri, Determination of scattering time and of valley occupation in transition-metal dichalcogenides doped by field effect, *Phys. Rev. B* **93**, 081407(R) (2016)
[36] K. S. Novoselov, D. Jiang, F. Schedin, T. J. Booth, V. V. Khotkevich, S. V. Morozov and A. K. Geim, Proceedings of the National Academy of Sciences of the United States of America **102**, 10451 (2005).
[37] M. M. Benameur, B. Radisavljevic, J. S. Heron, S. Sahoo, H. Berger and A. Kis, Visibility of dichalcogenide nanolayers. *Nanotechnology* **22**, 125706 (2011).
[38] Y. Fu, E. Liu, H. Yuan, P. Tang, B. Lian, G. Xu, J. Zeng, Z. Chen, Y. Wang, W. Zhou, K. Xu, A. Gao, C. Pan, M. Wang, B. Wang, S. C. Zhang, Y. Cui, H. Y. Hwang, and F. Miao, Gated tuned superconductivity and phonon softening in monolayer and bilayer MoS_2, *npj Quantum Mater.* **2**, 52 (2017)
[39] M. Kang, B. Kim, S. H. Ryu, S. W. Jung, J. Kim, L. Moreschini, C. Jozwiak, E. Rotenberg, A. Bostwick, and K. S. Kim, Universal Mechanism of Band-Gap Engineering in Transition-Metal Dichalcogenides, *Nano Lett.* **17**, 1610 (2017)
[40] R. Roldàn, E. Cappelluti, and F. Guinea, Interactions and superconductivity in heavily doped MoS_2, *Phys. Rev. B* **88**, 054515 (2013)
[41] T. Das and K. Dolui, Superconducting dome in MoS_2 and $TiSe_2$ generated by quasiparticle-phonon coupling, *Phys. Rev. B* **91**, 094510 (2015)
[42] Y. T. Hsu, A. Vaezi, M. H. Fischer, and E. A. Kim, Topological superconductivity in monolayer transition metal dichalcogenides, *Nat. Commun.* **8**, 14985 (2017)
[43] Y. Nakamura and Y. Yanase, Odd-parity superconductivity in bilayer transition metal dichalcogenides, *Phys. Rev. B* **96**, 054501 (2017)
[44] Z. Wu, S. Xu, H. Lu, A. Khamoshi, G. B. Liu, T. Han, Y. Wu, J. Lin, G. Long, Y. He, Y. Cai, Y. Yao, F. Zhang, and Ning Wang, Even-odd layer-dependent magnetotransport of high-mobility Q-valley electrons in transition metal disulfides, *Nat. Commun.* **7**, 12955 (2016)
[45] X. Cui, G. H. Lee, Y. D. Kim, G. Arefe, P. Y. Huang, C. H. Lee, D. A. Chenet, X. Zhang, L. Wang, F. Ye, F. Pizzocchero, B. S. Jessen, K. Watanabe, T. Taniguchi, D. A. Muller, T. Low, P. Kim, and J. Hone, Multi-terminal transport measurements of MoS_2 using a van der Waals heterostructure device platform, *Nat. Nanotechnol.* **10**, 534 (2015)
[46] Q. H. Chen, J. M. Lu, L. Liang, O. Zheliuk, A. Ali, P. Sheng, and J. T. Ye, Inducing and Manipulating Heteroelectronic States in a Single MoS_2 Thin Flake, *Phys. Rev. Lett.* **119**, 147002 (2017)
[47] W. E. Pickett, in *Emergent Phenomena in Correlated Matter*, edited by E. Pavarini, E. Koch, and U. Schollwöck, Forschungszentrum Jülich GmbH and Institute for Advanced Simulations, Jülich, Germany, 2013, pp. 5.10-5.11.
[48] M. Rösner, S. Haas, and T. O. Wehling, Phase diagram of electron-doped dichalcogenides, *Phys. Rev. B* **90**, 245105 (2014)
[49] C. Casiraghi, A. Hartschuh, E. Lidorikis, H. Qian, H. Harutyunyan, T. Gokus, K. S. Novoselov, and A. C. Ferrari, Rayleigh Imaging of Graphene and Graphene Layers, *Nano Lett.* **7**, 2711 (2007)
[50] J. L. Verble and T. J. Wieting, Lattice Mode Degeneracy in MoS_2 and Other Layer Compounds. *Phys. Rev. Lett.* **25**, 362 (1970).
[51] T. J. Wieting and J. L. Verble, Infrared and Raman Studies of Long-Wavelength Optical Phonons in Hexagonal MoS_2. *Phys. Rev. B* **3**, 4286 (1971).
[52] C. Lee, H. G. Yan, L. E. Brus, T. F. Heinz, J. Hone and S. Ryu, Anomalous Lattice Vibrations of Single- and Few-Layer MoS_2. *ACS Nano* **4**, 2695 (2010).
[53] A. M. Stacy and D. T. Hodul, Raman spectra of IVB and VIB transition metal disulfides using laser energies

near the absorption edges. *J. Phys. Chem. Solids* **46**, 405 (1985).

[54] X. Zhang, W. P. Han, J. B. Wu, S. Milana, Y. Lu, Q. Q. Li, A. C. Ferrari and P. H. Tan, Raman spectroscopy of shear and layer breathing modes in multilayer MoS_2. *Phys. Rev. B* **87**, 115413 (2013).

[55] Y. Yu, F. Yang, X. F. Lu, Y. J. Yan, Y.-H. Cho, L. Ma, X. Niu, S. Kim, Y.-W. Son, D. Feng, S. Li, S.-W. Cheong, X. H. Chen, and Y. Zhang, Gate-tunable phase transitions in thin flakes of 1T-TaS_2, *Nat. Nanotechnol.* **10**, 270 (2015)

[56] P. H. Tan, W. P. Han, W. J. Zhao, Z. H. Wu, K. Chang, H. Wang, Y. F. Wang, N. Bonini, N. Marzari, N. Pugno, G. Savini, A. Lombardo, and A. C. Ferrari, The shear mode of multilayer graphene. *Nat. Mater.* **11**, 294 (2012)

[57] W. Shi, J. T. Ye, Y. Zhang, R. Suzuki, M. Yoshida, J. Miyazaki, N. Inoue, Y. Saito, and Y. Iwasa, Superconductivity Series in Transition Metal Dichalcogenides by Ionic Gating, *Sci. Rep.* **5**, 12534 (2015)

[58] X. X. Xi, H. Berger, L. Forró, J. Shan, and K. F. Mak, Gate Tuning of Electronic Phase Transitions in Two-Dimensional $NbSe_2$, *Phys. Rev. Lett.* **117**, 106801 (2016)

[59] J. T. Ye, M. F. Craciun, M. Koshino, S. Russo, S. Inoue, H. T. Yuan, H. Shimotani, A. F. Morpurgo, and Y. Iwasa, Accessing the transport properties of graphene and its multilayers at high carrier density. *Proc. Natl. Acad. Sci. USA* **108**, 32 (2011)

[60] R. S. Gonnelli, E. Piatti, A. Sola, M. Tortello, F. Dolcini, S. Galasso, J. R. Nair, C. Gerbaldi, E. Cappelluti, M. Bruna, and A. C. Ferrari, Weak localization in electric-double-layer gated few-layer graphene, *2D Mater.* **4**, 035006 (2017)

[61] E. Piatti, S. Galasso, M. Tortello, J. R. Nair, C. Gerbaldi, M. Bruna, S. Borini, D. Daghero, and R. S. Gonnelli, Carrier mobility and scatterig lifetimes in electric-double-layer gated few-layer graphene, *Appl. Surf. Sci.* **395**, 37 (2017)

[62] E. Piatti, Q. Chen, and J. T. Ye, Strong dopant dependence of electric transport in ion-gated few-layer MoS_2, *Appl. Phys. Lett.* **111**, 013106 (2017)

[63] F. Bonaccorso, A. Lombardo, T. Hasan, Z. P. Sun, L. Colombo, and A. C. Ferrari, Production and processing of graphene and 2d crystals. *Mater. Today* **15**, 564 (2012)

[64] K. S. Novoselov, D. Jiang, F. Schedin, T. J. Booth, V. V. Khotkevich, S. V. Morozov, and A. K. Geim, Two-dimensional atomic crystals. *Proc. Natl. Acad. Sci. USA* **102**, 10451 (2005)

[65] H. Li, J. Wu, X. Huang G. Lu, J. Yang, X. Lu, Q. Xiong, and H. Zhang, Rapid and Reliable Thickness Identification of Two-Dimensional Nanosheets Using Optical Microscopy, *ACS Nano* **7**, 10344 (2013)

[66] P. Gallagher, M. Y. Lee, T. A. Petach, S. W. Stanwyck, J. R. Williams, K. Watanabe, T. Taniguchi, and D. Goldhaber-Gordon, A high-mobility electronic system at an electrolyte-gated oxide surface, *Nat. Commun.* **6**, 6437 (2015)

[67] D. Ovchinnikov, F. Gargiulo, A. Allain, D. J. Pasquier, D. Dumcenco, C. H. Ho, O. V. Yazyev, and A. Kis, Disorder engineering and conductivity dome in ReS2 with electrolyte gating, *Nat. Commun.* **7**, 12391 (2016)

[68] I. M. Lifshitz, Anomalies of electron characteristics of a metal in the high pressure region, *J. Exp. Theor. Phys.* **11**, 1130 (1960)

[69] N. Podberezskaya, S. Magarill, N. Pervukhina, and S. Borisov, Crystal Chemistry of Dichalcogenides MX_2, *J. Struct. Chem.* **42**, 654 (2001)

[70] A. Molina-Sánchez and L. Wirtz, Phonons in single-layer and few-layer MoS_2 and WS_2, *Phys. Rev. B* **84**, 155413 (2011)

[71] C. Ataca, M. Topsakal, E. Aktürk, and S. Ciraci, A Comparative Study of Lattice Dynamics of Three- and Two-Dimensional MoS_2, *J. Phys. Chem. C* **115**, 16354 (2011)

[72] R. S. Gonnelli, D. Daghero, M. Tortello, G. A. Ummarino, Z. Bukowski, J. Karpinski, P. G. Reuvekamp, R. K. Kremer, G. Profeta, K. Suzuki and K. Kuroki, Fermi-Surface Topological Phase Transition and Horizontal Order-Parameter Nodes in $CaFe_2As_2$ Under Pressure, *Sci. Rep.* **6**, 26394 (2016)

[73] P. B. Allen and R. C. Dynes, Transition temperature of strong-coupled superconductors reanalyzed, *Phys. Rev. B* **12**, 905 (1975)

[74] D. Daghero, F. Paolucci, A. Sola, M. Tortello, G. A. Ummarino, M. Agosto, R. S. Gonnelli, J. R. Nair, and C. Gerbaldi, Large conductance modulation of gold thin films by huge charge injection via electrochemical gating, *Phys. Rev. Lett.* **108**, 066807 (2012)

[75] B. El-Kareh, in *Fundamentals of Semiconductor Processing Technologies*, Kluwer Academic Publishers (1995)

[76] G. Grüner, *Density Waves In Solids* (Westview, 2009)

[77] M. Kutz, *Handbook of materials selection*, (John Wiley & Sons, 2002)

[78] D. Yoon, Y-.W. Son, and H. Cheong, Negative thermal expansion coefficient of graphene measured by Raman spectroscopy, *Nano Lett.* **11**, 3227 (2011)

[79] T. M. G. Mohiuddin, A. Lombardo, R. R. Nair, A. Bonetti, G. Savini, R. Jalil, N. Bonini, D. M. Basko, C. Galiotis, N. Marzari, K. S. Novoselov, A. K. Geim, and A. C. Ferrari, Uniaxial strain in graphene by Raman spectroscopy, *Phys. Rev. B* **79**, 205433 (2009)

[80] C. K. Gan and Y. Y. F. Liu, Direct calculation of the linear thermal expansion coefficients of MoS_2 via symmetry-preserving deformations. *Phys. Rev. B* **94**, 134303 (2016)

[81] Standard Reference Material 739 Certificate; National Institute of Standards and Technology: Gaithersburg, MD (1991)

[82] F. C. Nix and D. MacNair, The thermal expansion of pure metals: copper, gold, aluminum, nickel, and iron. *Phys. Rev.* **60**, 597 (1941)

[83] P. G. Klemens, Anharmonic decay of optical phonons. *Phys. Rev.* **148**, 845 (1966)

[84] J.-U. Lee, S. Woo, J. Park, H. C. Park, Y.-W. Son, and H. Cheong, Strain-shear coupling in bilayer MoS_2. *Nat. Commun.* **8**, 1370 (2017)

[85] H. J. Conley, B. Wang, J. I. Ziegler, R. F. Haglund Jr., S. T. Pantelides, and K. I. Bolotin, Bandgap engineering of strained monolayer and bilayer MoS_2. *Nano Lett.* **13**, 3626 (2013)